Acoustic solitons in waveguides with Helmholtz resonators: Transmission line approach

V. Achilleos,[1] O. Richoux,[2] G. Theocharis,[2] and D. J. Frantzeskakis[1]

[1]*Department of Physics, University of Athens, Panepistimiopolis, Zografos, Athens 15784, Greece*

[2]*LUNAM Université, Université du Maine, CNRS, LAUM UMR 6613, Av. O. Messiaen, 72085 Le Mans, France*

We report experimental results and study theoretically soliton formation and propagation in an air-filled acoustic waveguide side loaded with Helmholtz resonators. We propose a theoretical modeling of the system, which relies on a transmission-line approach, leading to a nonlinear dynamical lattice model. The latter allows for an analytical description of the various soliton solutions for the pressure, which are found by means of dynamical systems and multiscale expansion techniques. These solutions include Boussinesq-like and Korteweg-de Vries pulse-shaped solitons that are observed in the experiment, as well as nonlinear Schrödinger envelope solitons, that are predicted theoretically. The analytical predictions are in excellent agreement with direct numerical simulations and in qualitative agreement with the experimental observations.

PACS number(s): 43.25.+y, 43.25.Rq, 05.45.Yv

I. INTRODUCTION

Solitons, namely robust localized waves propagating undistorted in nonlinear dispersive media [1–3], have been studied extensively in various physical contexts. Indeed, soliton formation, stability, dynamics, and interactions have been analyzed, both in theory and in experiments, in water waves [4,5], plasma physics [5], nonlinear optics [6], atomic Bose-Einstein condensation (BEC) [7], and so on.

On the other hand, solitons have also been studied in acoustics, both in solids and in fluids [8]. In particular, nonlinear solitary waves have been the subject of many studies over the past few years in granular chains [9] and crystalline solids (see Ref. [10], and references therein). In the latter case, solitons and solitary waves in crystals and their surfaces have been attained by nanosecond and picosecond laser ultrasonics methods. However, solitons in fluids have been studied less extensively: In fact, pertinent studies include seminal work by Sugimoto and coworkers, who studied theoretically [11–13] and demonstrated experimentally [12,13] propagation of one-dimensional (1D) acoustic solitary waves in an air-filled waveguide, with a periodic array of Helmholtz resonators. In these works, the analysis was based on nonlinear wave equations with fractional derivative terms accounting for losses. For this model, soliton solutions were found in an implicit form and turned out to be close to Korteweg-de Vries (KdV) solitons in some asymptotic limit; additionally, numerical studies on the model proposed in Refs. [11–13] were recently reported, too [14]. Other relevant works include Refs. [15], where diffusive soliton solutions to the so-called Kuznetsov equation (which models weakly nonlinear acoustic wave propagation in viscoelastic media) were studied. Note that traveling wave solutions of a higher-order nonlinear acoustic wave equation of the Kuznetsov type (valid for larger values of acoustic Mach number) were rigorously studied as well [16]. It is also relevant to mention the work of Ref. [17], where envelope solitons (holes) were predicted to occur in cylindrical acoustic waveguides (in this system, higher-order dispersive modes were taken into account).

In this work, we revisit the theme of a lattice made of Helmholtz resonators side connected to a tube [18]. We present experimental observations of acoustic solitons in this setting

and propose an analytically tractable modeling, relying on an effective nonlinear transmission line (TL) description of the system. Our approach allows for both an efficient description of the relevant experimental findings and the prediction of other localized nonlinear structures that can be supported in the system.

Generally speaking, the TL approach is a powerful tool commonly used in electromagnetic (EM) wave applications [19] and has recently gained considerable attention due to its applicability in the analysis and design of both EM [20] and acoustic [21–23] metamaterials. This approach also allows for the study of nonlinear effects, and particularly soliton formation and propagation, a theme that has been studied extensively in the past in the context of electrical TLs [2] and more recently in the realm of TL metamaterials [24].

In our setting, namely the 1D lattice of Helmholtz resonators, the proposed TL model correctly reproduces—in the linear limit—the dispersion relation. Furthermore, in the nonlinear regime, and in the small-amplitude, long-wavelentgth limit, the TL model describes—in a good agreement with the experiment—the soliton propagation in the waveguide. This simplified model also allows for an analytical study of the solitary waves based on universal nonlinear evolution equations that are derived by means of asymptotic expansions (see below). A direct numerical integration of the model provides numerical results that are consistent with the analytics and the experimental observations. Additionally, in the framework of the TL model, it is also possible to predict the formation of envelope solitons (both of the bright and the dark type).

We now proceed with a more specific description of our analysis and findings. First, we note that our analysis relies on the study of an electrical TL, as per the electroacoustic analogy, where the voltage corresponds to the acoustic pressure and the current to the volume velocity flowing through the waveguide's cross-sectional area [25]. Nonlinear effects are taken into consideration by incorporating nonlinear elements into the unit-cell circuit, accounting for the dependence of wave celerity on the pressure (note that Helmholtz resonators are assumed to have a linear response, while nonlinearity originates only for the large-amplitude wave propagation within the waveguide). This representation allows for the derivation of a nonlinear lattice model, which is studied

numerically and analytically. In the numerical simulations, using initial conditions relevant to our experiments, we are able to reproduce soliton profiles and characteristics (speed, width, etc.) in a good agreement with the experimental observations. Furthermore, employing the continuum approximation, we study analytically the lattice model and show that it is intimately related (in proper temporal and spatial scales) to models that have been studied in the past in other branches of physics: These include a Boussinesq-type model and a KdV equation (originally used to describe shallow-water waves [3,4], waves in plasmas [5], solitons in electrical TLs [2], etc.), as well as a nonlinear Schrödinger (NLS) equation (describing deep-water waves [3,4], optical solitons [1–3,6], dynamics of BEC [7], etc.). This way, we derive approximate pulselike solitons of the Boussinesq and KdV type, as well as bright and dark envelope solitons satisfying an effective NLS equation. In all cases, we identify parameter regimes where different types of solitons can be formed and present numerical results that are found to be in an excellent agreement with the analytical predictions.

The paper is structured as follows. In Sec. II, we describe the experimental setup and present experimental results for the formation of acoustic solitons in the 1D lattice of Helmholtz resonators. We also introduce our model and, by employing the TL approach, derive the nonlinear lattice equation and compare numerical findings for the latter with relevant experimental results. Section III is devoted to our analytical study: There we present the various types of solitons that can be formed in our setting, identify relevant parameter regimes and spatiotemporal scales, and investigate their propagation characteristics. Finally, in Sec. IV, we present our conclusions and discuss future research directions.

II. THE HELMHOLTZ RESONATOR LATTICE

A. Experimental setup and observations

We start by presenting our experimental setup, which consists of a long cylindrical waveguide, of length $L = 6$ m, with a cross section $S = \pi R^2$ with an inner radius $R = 25 \times 10^{-3}$ m and a 5×10^{-3} m thick wall. This waveguide is connected to an array of 60 Helmholtz resonators, which are periodically distributed. The distance between two consecutive resonators is $d = 0.1$ m. Each resonator is composed by a neck (cylindrical tube with an inner radius $r = 10 \times 10^{-3}$ m and a length $\ell = 20 \times 10^{-3}$ m) and a variable-length cavity (cylindrical tube with an inner radius $r_v = 21.5 \times 10^{-3}$ m and a maximum length $h = 165 \times 10^{-3}$ m). Notice that the end of the waveguide, located at $d/2$ from the last resonator, is rigidly closed.

The input signal is generated by the explosion of a balloon. The balloon is located at 20 cm of the lattice into a waveguide connected to the main tube and is inflated until its explosion. The produced acoustic wave is measured with 2 $PCB106B$ microphones, carefully calibrated, which are located 20 cm in front of the lattice and at the end of lattice (the microphone is embedded in the rigid end); recall that the propagation distance is $L = 6.2$ m. The experimental setup is shown in Fig. 1.

Figure 2(a) shows the temporal profiles of the normalized acoustic pressure measured at the first microphone located 20 cm before the first resonator ($x = 0$ m). The input signal,
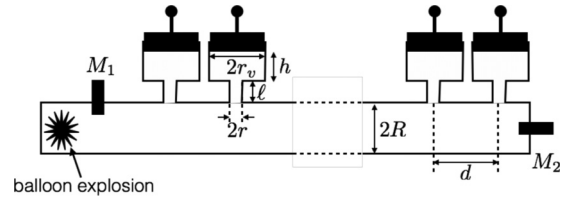

FIG. 1. Schematic illustration of the experimental setup.

generated by the balloon explosion, can be described by a gate signal with a large amplitude (around 30 kPa) and a width around 1.5 ms. Figures 2(b), 2(c), and 2(d) present the temporal profiles of the acoustic pressure measured after a 6-m propagation in the Helmholtz resonators lattice ($x = 6.2$ m) for the cases of $h = 0.02$ m, $h = 0.07$ m, and $h = 0.165$ m, respectively. Oppositely to the case of a waveguide without resonators where a shock wave is formed [13,26], we observe the propagation of a wave with a smooth shape through the lattice. The characteristics of this wave, namely shape, amplitude, and velocity, are strongly dependent on the cavity length of the resonators, which defines the dispersion characteristics of the lattice (see Sec. III.B). As shown, for $h = 0.07$ m and $h = 0.165$ m, the wave shape is clearly symmetrical, while for $h = 0.02$ m this is not the case. Generally, it is observed that the competition between nonlinearities (due to a cumulative effect occurring for large amplitude pulse input) and dispersion in the medium (due to the presence of Helmholtz resonators) produces waves of constant shape, with amplitude-dependent velocity, which are in fact acoustic solitons (note that we use the term "soliton" in a loose sense, without implying complete integrability [3]).

B. The discrete model: Transmission line approach

Next, in order to model our system and provide theoretical results for the above experimental observations of acoustic
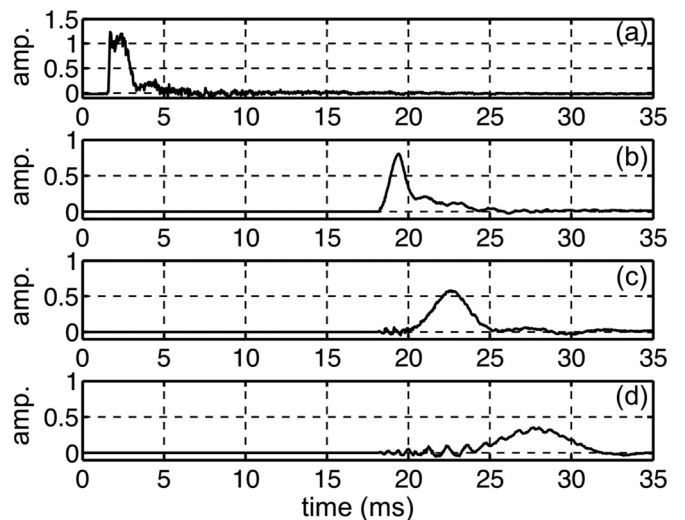

FIG. 2. Panel (a) shows the initial acoustic pressure, measured at $x = 0$ m. Panels (b), (c), and (d) show, respectively, the acoustic pressure measured at the end of the lattice ($x = 6.2$ m) for resonator cavity length $h = 0.02$ m, $h = 0.07$ m, and $h = 0.165$ m.

solitons, we will employ the TL approach. Our starting point relies on the consideration of an ideal fluid, and use of the fluid-dynamic equations, neglecting viscosity and other dissipative terms. If we restrict our analysis to 1D flow—as in the case of the experimental results of Fig. 2—wave propagation is described by the following equations:

$$\frac{\partial \varrho}{\partial t} + \frac{\partial}{\partial x}(\varrho v) = 0, \tag{1}$$

$$\frac{\partial v}{\partial t} + v\frac{\partial v}{\partial x} = -\frac{1}{\varrho}\frac{\partial p}{\partial x}, \tag{2}$$

where $\varrho(p,s)$ is the fluid mass density, s is the entropy, v is the acoustic fluid velocity, and p is the acoustic pressure. We assume that the entropy s is constant, while the mass density ϱ and wave celerity $c \equiv (\partial p/\partial \varrho)^{1/2}$ are considered as functions of the total pressure p. Accordingly, the acoustic fluid velocity v can can be written as a single-valued function of the pressure p so $\partial v/\partial t = (dv/dp)\partial p/\partial t$. We wish to model the acoustic propagation along the waveguide in the low-frequency regime, where only plane waves can propagate, by means of the electroacoustic analogy [25]. Considering the long-wavelength limit, the mass conservation and Euler's equations (1) and (2) between two points separated by dx (much smaller than the acoustic wavelength) can be approximated as:

$$u_n = C_w\frac{\partial p_{n+1}}{\partial t} + u_{n+1}, \tag{3}$$

$$p_n = L_w\frac{\partial u_{n+1}}{\partial t} + p_{n+1}, \tag{4}$$

where u is the acoustic volume velocity and the subscripts n and $n + 1$ are related, respectively, to left and right sides of the tube at some point dx. According to the electrical analogy, the propagation along a unit cell with length dx can be modelled by a simple electrical circuit for the "current" u_n and the "voltage" p_n, consisting of an inductance L_w and a capacitance C_w. In the linear regime, these are given by:

$$L_{w0} = \varrho_0 dx/S, \quad C_{w0} = Sdx/\varrho_0 c_0^2, \tag{5}$$

where ϱ_0 is the density evaluated at the equilibrium state and c_0 is the speed of sound. Notice that in the nonlinear regime L_w and C_w can define a wave celerity as $c_{NL}^2 = 1/L_w C_w$. For our analysis below, we will assume that the inductance is linear, $L_w = L_{w0}$, while the capacitance defined as $C_w = Sdx/\varrho_0 c_{NL}^2$ is nonlinear, depending on the pressure p; this choice relies on the approximation that (to a first order) the density does not depend on p, while the wave celerity c_{NL} depends on p.

In order to model the experimental setup that incorporates the Helmholtz resonators, we will include an additional parallel branch in the unit-cell circuit, composed by a serial combination of an inductance L_H and a capacitance C_H, as shown in Fig. 3. We consider the response of the Helmholtz resonators to be linear. Nonlinearity originates only from the large-amplitude acoustic propagation within the waveguide. Thus, in the low-frequency approximation, the relevant inductance and capacitance are given by $L_H = \varrho_0 \ell/S_n$ and $C_H = V_H/\varrho_0 c_0^2$, respectively, where ℓ, S_n, and V_H are the length and the cross-sectional area of the resonator neck, and
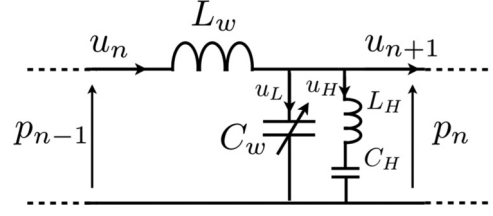

FIG. 3. The unit-cell circuit of the nonlinear Helmholtz lattice model.

the total volume of the resonator cavity, respectively. Notice that by including a resonator in each unit cell, it is natural to set $dx = d$ (recall that d is the distance between two successive resonators).

Using the unit-cell circuit of Fig. 3, we can now use Kirchhoff's voltage and current laws and derive an evolution equation for the pressure p_n in the n-th cell of the lattice. Let us first consider the Kirchhoff's voltage law for two successive cells, which yields:

$$p_{n-1} - p_n = L_w\frac{d}{dt}u_n, \tag{6}$$

$$p_n - p_{n+1} = L_w\frac{d}{dt}u_{n+1}. \tag{7}$$

Subtracting the above equations, we obtain the difference equation:

$$\hat{\delta}^2 p_n = \hat{\mathcal{L}}(u_n - u_{n+1}), \tag{8}$$

where $\hat{\delta}^2 p_n \equiv p_{n+1} - 2p_n + p_{n-1}$ and $\hat{\mathcal{L}} \equiv L_w d/dt$. On the other hand, Kirchhoff's current law yields:

$$u_n - u_{n+1} = \frac{d}{dt}(C_w p_n) + \hat{P}^{-1}\frac{dp_n}{dt}, \tag{9}$$

where the first and second terms in the right-hand side denote the currents across the capacitance C_w and the Helmholtz branch, respectively, with $\hat{P}^{-1}$ being the inverse of the operator $\hat{P} \equiv L_H d^2/dt^2 + 1/C_H$.

Substituting Eq. (9) into Eq. (8), we obtain the following equation for the pressure p_n:

$$L_w C_H\frac{d^2 p_n}{dt^2} - \left(1 + L_H C_H\frac{d^2}{dt^2}\right)\hat{\delta}^2 p_n$$
$$+ L_w\frac{d^2}{dt^2}\left(1 + L_H C_H\frac{d^2}{dt^2}\right)(C_w p_n) = 0, \tag{10}$$

where we note that the capacitance C_w depends on the pressure. In order to quantify this dependence, and take into account the nonlinear processes in the propagation, we can add a nonlinear term in the celerity as [25,27]:

$$c_{NL} \approx c_0\left(1 + \beta_0 p/\varrho_0 c_0^2\right), \tag{11}$$

where $c_0 = 343.26$ m/s is the speed of sound at room temperature and $\beta_0 = 1.2$ for the case of air. Then the second of Eqs. (5) leads to the following pressure-dependent capacitance C_w:

$$C_w(p_n) \approx C_{w0} + C_w' p_n, \tag{12}$$

where $C_{w0} = Sd/\varrho_0 c_0^2$ is a constant capacitance (relevant to the linear case) and $C_w' = -2\frac{\beta_0}{\varrho_0 c_0^2} C_{w0}$.

Substituting Eq. (12) into Eq. (10), we obtain the equation:

$$\frac{d^2 p_n}{dt^2} - \frac{c_0^2}{\kappa d^2}\left(1 + \frac{1}{\omega_0^2}\frac{d^2}{dt^2}\right)\hat{\delta}^2 p_n + \frac{1}{\kappa}\frac{d^2}{dt^2}\left(1 + \frac{1}{\omega_0^2}\frac{d^2}{dt^2}\right)$$

$$\times\left[p_n\left(1 - 2\frac{\beta_0}{\varrho_0 c_0^2}p_n\right)\right] = 0, \quad (13)$$

where $\omega_0 = c_0\sqrt{S_n/S_v h\ell}$ is the Helmholtz resonance frequency ($S_n = \pi r^2$ and $S_v = \pi r_v^2$ are the cross-sectional areas of the resonator neck and cavity, respectively) and $\kappa = V_H/V$ is a geometrical factor (ratio of the volume of the Helmholtz resonator V_H over the tube volume V in a unit cell of length d), and we have used the following equations connecting the transmission line parameters with the acoustic waveguide characteristics:

$$L_w C_H = \frac{\kappa}{d^2 c_0^2}, \quad L_H C_H = \frac{1}{\omega_0^2}, \quad L_w C_{w0} = \frac{d^2}{c_0^2}, \quad (14)$$

where L_w is also evaluated at $\varrho = \varrho_0$. The above nonlinear dynamical lattice equation is one of the main results of the present work: It describes the propagation of acoustic waves in a tube with an array of Helmholtz resonators. This simplified model will be used below in order to derive analytical solitary wave solutions that are supported in this setting—as is also evident from the experimental results shown in Fig. 2.

C. Comparison with the experiment

Let us now proceed by comparing results that can be derived in the framework of the lattice model (13) with the experimental results presented above.

We numerically integrate Eq. (13) by means of a 4th-order Runge-Kutta method, using an initial condition similar to the experiments, as shown in the top panel of Fig. 2. In particular, we use a super-Gaussian pulse of the form

$$p_{n=0}(t) = A\exp[-((t - t_0)/w_0)^{16}], \quad (15)$$

of amplitude $A = 30$ kPa and width $w_0/2 = 400$ Hz. The values of the coefficients of the various terms of Eq. (13) depend actually only on the cavity length h, since all other parameters are fixed.

The results of the direct numerical simulations, corresponding to the three different cavity lengths used in the experiment ($h = 0.02, 0.07, 0.165$ m), are shown in Fig. 4. In all cases shown in Figs. 4(b)–4(d), the profile of each pulse is shown for the lattice cite $n = 60$, corresponding to a distance 6 m from the first resonator. The profiles in Figs. 4(b)–4(d) are time shifted by $\Delta t \approx 0.9$ ms corresponding to the propagating time needed for the initial pulse to reach the first resonator; this is done to facilitate direct comparison with the experimental results of Fig. 2.

Comparing corresponding panels of Figs. 2 and 4 for each of the three different values of h, it is seen that the solitary waves obtained numerically via Eq. (13) have approximately the same width as those observed in the experiment. Notice that quantitative differences between numerical and experimental soliton amplitudes, as well as the presence of "tails" attached
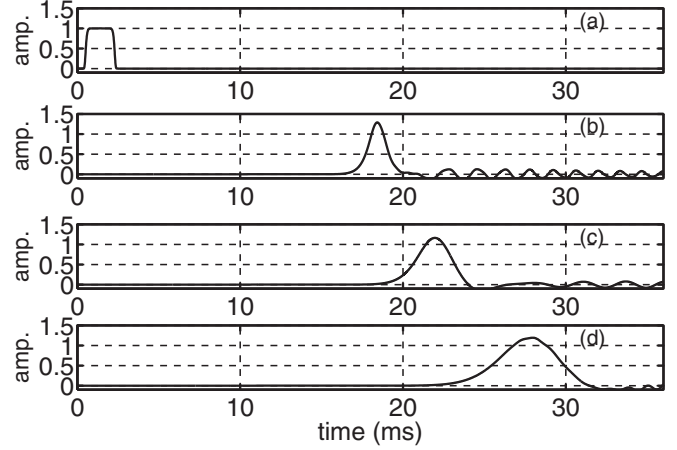

FIG. 4. Top panel: Initial condition p_0 used for the numerical integration of Eq. (13). Rest of the panels (time shifted by 0.9 ms, see text) show the pressure at $n = 60$ as a function of time for the same value of the cavity length as in the respective experimental data (cf. Fig. 2).

to the solitons (which are absent in the experimental data), may be qualitatively understood by (i) the presence of losses in the experiment [which are not included in the simplified model of Eq. (13)] and (ii) the fact that the initial conditions used in the experiment and simulations differ.

In any case, the above comparison shows that Eq. (13) can be used to describe, in a fairly good agreement with the experiment, the formation of acoustic solitary waves. Below we will show that, using this simplified model, we can obtain analytically different types of acoustic solitons in different experimentally relevant regimes.

III. ACOUSTIC SOLITONS

A. The continuum approximation

For our analytical considerations, we will focus on the continuum limit of Eq. (13), corresponding to $n \to \infty$ and $d \to 0$ (but with nd being finite); in such a case, the pressure becomes $p_n(t) \to p(x,t)$, where $x = nd$ is a continuous variable. Then the difference operator $\hat{\delta}^2$ is approximated by $\hat{\delta}^2 p_n \approx d^2 p_{xx}$, where terms of the order $\mathcal{O}(d^4)$ and higher are neglected, and subscripts denote partial derivatives. It is also convenient to express our model in dimensionless form; this can be done upon introducing the normalized variables χ and τ and normalized pressure P [of order $\mathcal{O}(1)$], which are defined as follows:

$$\tau = \tilde{\omega}_0 t, \quad \chi = \frac{\tilde{\omega}_0}{c_0\sqrt{\alpha}}x, \quad \frac{p}{p_0} = \epsilon P, \quad (16)$$

where $\tilde{\omega}_0$ is a characteristic spectral width or inverse temporal width (which is set by the initial condition), $p_0 = \varrho_0 c_0^2/2\beta_0$, $\alpha = 1/(1 + \kappa)$, and ϵ is a dimensionless small parameter ($\epsilon \ll 1$), defining the strength of the nonlinearity. In these variables, the continuum limit of Eq. (13) reads:

$$P_{\tau\tau} - P_{\chi\chi} - \Omega^2(P_{\chi\chi\tau\tau} - \alpha P_{\tau\tau\tau\tau})$$

$$- \epsilon\alpha[(P^2)_{\tau\tau} + \Omega^2(P^2)_{\tau\tau\tau\tau}] = 0, \quad (17)$$

where $\Omega = \tilde{\omega}_0/\omega_0$. Equation (17) is a Boussinesq-like model, which has been originally proposed for studies of solitons in shallow water [3,4] but later was used in studies of solitons in different contexts, including electrical TLs [2]. In our case, the dispersion terms of Eq. (17) are due to the presence of Helmholtz resonators, and their strength is measured by the dimensionless parameter Ω. The strength of the nonlinear terms, on the other hand, is set by the parameter ϵ. Notice that in the absence of the Helmholtz resonators, i.e., for $\omega_0 \to \infty$ and $\kappa = 0$ (i.e., $\Omega = 0$ and $\alpha = 1$), Eq. (17) is reduced to the well-known Westervelt equation, which is a common nonlinear model describing 1D acoustic wave propagation [27].

B. Linear theory

We start by considering the linear limit of Eq. (17) and the respective dispersion relation. Note that in the limit of $\epsilon \to 0$, Eq. (17) is reduced to the linear wave equation (in the lossless case) studied in Ref. [28] [see Eq. (61) of this work].

Assuming propagation of plane waves in the lattice, of the form $P \propto \exp[i(k\chi - \omega\tau)]$, we obtain the following dispersion relation connecting the wave number k and frequency ω:

$$D(\omega,k) \equiv k^2 - \omega^2 - \Omega^2(k^2\omega^2 - \alpha\omega^4) = 0. \qquad (18)$$

Since all quantities in the above dispersion relation are dimensionless, it is also relevant to express Eq. (18) in physical units. In particular, taking into regard that the frequency ω_{ph} and wave number k_{ph} in physical units are connected with their dimensionless counterparts through $\omega = \omega_{\mathrm{ph}}/\tilde{\omega}_0$ and $k = k_{\mathrm{ph}}c_0\sqrt{\alpha}/\tilde{\omega}_0$, we can express Eq. (18) in the following form:

$$k_{\mathrm{ph}}^2 - \frac{\omega_{\mathrm{ph}}^2}{c_0^2\alpha} - \frac{1}{\omega_0^2}\left(k_{\mathrm{ph}}^2\omega_{\mathrm{ph}}^2 - \frac{\omega_{\mathrm{ph}}^4}{c_0^2}\right) = 0. \qquad (19)$$

Solving Eq. (19) analytically with respect to k_{ph}, we then can determine the frequency $f = \omega_{\mathrm{ph}}/2\pi$ as a function of the normalized wave number $k_{\mathrm{ph}}d$ and plot the resulting dispersion relation. The relevant result is depicted in Fig. 5 by the dotted (black) line for the three different values of the Helmholtz resonator cavity length h used in the experiment, namely $h = 0.02$ m, $h = 0.07$ m, and $h = 0.165$ m.

On the other hand, the solid (green) line in the same figure shows the respective result (for the lossless case under consideration) for the dispersion relation, as obtained using Bloch theory and the transfer matrix method [28]:

$$\cos(k_{\mathrm{ph}}d) = \cos\left(\frac{\omega_{\mathrm{ph}}}{c_0}d\right) + i\frac{Z_0}{2Z_b}\sin\left(\frac{\omega_{\mathrm{ph}}}{c_0}d\right), \qquad (20)$$

where Z_b is the input impedance of the Helmholtz resonator branch and $Z_0 = \varrho_0 c_0/S$ is the acoustic characteristic impedance of the waveguide; for the lossless case $Z_b = i(\omega_{\mathrm{ph}}L_H - 1/\omega_{\mathrm{ph}}C_H)$. Note that, in the linear regime, the transmission line approach to acoustic waveguides with periodically arranged Helmholtz resonators has also been proposed and discussed in other works (see, e.g., Refs. [22,23]).

The dispersion relation (20) obviously reflects the periodicity of the system, featuring a band-gap structure. This becomes clear upon observing the upper gap shown in Fig. 5, which originates from Bragg-type constructive interference of reflections and is characterized by the Bragg frequency
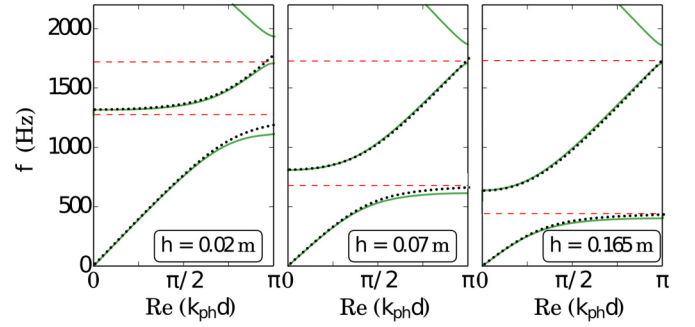

FIG. 5. (Color online) The dispersion relation, expressed in physical units, as obtained via Eq. (20) [solid (green) line] for three different values of the Helmholtz resonator cavity length h. This result is compared to the approximate one of Eq. (19) [dotted (black) line]. The lower and upper horizontal dashed (red) lines depict the Helmholtz resonance frequency $f_0 = \omega_0/2\pi$ and the Bragg frequency f_B, respectively. Note that f_0 takes the values 1270 Hz ($h = 0.02$ m), 679 Hz ($h = 0.07$), and 442 Hz ($h = 0.165$ m), while in all cases f_B is fixed from the lattice constant $d = 0.1$ m and takes the value $f_B = c_0/2d = 1720$ Hz.

$f_B = c_0/2d$; the latter is equal to 1720 Hz for our setting and is depicted by the upper dashed (red) lines in the three panels of Fig. 5. In addition, the dispersion relation features still another gap (usually called "resonator" or "hybridization" band gap), originating from Fano resonances or interference, due to the presence of the Helmholtz resonators. This gap is around the resonance frequency of the Helmholtz resonator, $f_0 = \omega_0/2\pi$, which is chosen to be sufficiently smaller than the Bragg frequency f_B; such a choice is possible by properly fixing the cavity length h. The location of f_0 for the three different values of h that are used in the experiment is depicted by the lower dashed (red) lines in the three panels of Fig. 5. Observing the structure of the first (lower) band, it is clear that by increasing the Helmholtz cavity length the resonance frequency decreases, and, additionally, the dispersion in the low-frequency regime increases. On the other hand, observing the structure of the second band, it is evident that the increase of the Helmholtz cavity length results in a decrease of dispersion near the Brillouin boundary.

Comparing the dispersion relation (20) with the one resulting from the continuum approximation [cf. Eq. (19)], we find a very good agreement between the two, especially in the regime of low frequencies (note that in this regime the transmission line approach is expected to be more accurate). In particular, the dispersion relation (19) is able to follow the lower band, the first gap, and the second band, especially in the regime of $k_{\mathrm{ph}}d \ll 1$ (where the continuum approximation is formally more accurate). For instance, the upper band gap edge for $k_{\mathrm{ph}} = 0$ is found from Eq. (19) as $\omega_{\mathrm{ph}} = \omega_0/\sqrt{\alpha}$, which is in agreement with the effective medium approach of Ref. [22].

In addition, the result of the continuum approximation is still in reasonable agreement with the result of Eq. (20) for moderate and larger values of $k_{\mathrm{ph}}d$, even sufficiently close to the Brillouin boundary. For the lower band, this agreement can be attributed to the fact that the first gap is only due to the Helmholtz resonance and not due to the system's periodicity. In

other words, dispersion only comes into play due to Helmholtz resonance [recall that dispersion in Eq. (17) vanishes for $\Omega = 0$ or $\omega_0 \to \infty$]. As concerns the second band, it can be observed that, for sufficiently large k_{ph}, the dispersion relation (19) becomes $\omega_{ph} = k_{ph} c_0$ for every cavity length h. The same behavior is also found from Eq. (20), which can explain the agreement with Eq. (19), even close to the Brillouin boundary (at least for the parameter values used in the experiment). There, it is obvious that the continuum approximation becomes invalid, because the dispersion relation (19) does not take into regard the periodicity of the system, thus failing to capture the band gap around f_B (as well as the structure of the spectrum for $f > f_B$). Notice that this failure is more pronounced for smaller values of cavity length (cf. left panel of Fig. 5) due to the fact that, in this case, periodicity-induced dispersion is enhanced.

Thus, concluding this section, the continuum approximation Eq. (17) is quite accurate in capturing the (Helmholtz resonance-induced) dispersion properties of the system in the low-frequency and long-wavelength regimes—as is the case for the parameter values used in the experiment. It is thus reasonable to expect that different types of solitons may be obtained in different regimes of the dispersion relation by exploiting the relative strength between dispersion and nonlinearity. A relevant study is appended in the following sections.

C. Boussinesq and KdV pulselike solitons

First we focus on the regime where the dispersion and nonlinearity terms of Eq. (17) are of the same order, i.e., $\epsilon \sim \Omega^2$. Given that we have already assumed a weak nonlinearity, it is obvious that the last term in the left-hand side of Eq. (17), which is $\propto \epsilon \Omega^2$, can be neglected. In such a case, Eq. (17) is reduced to the following equation:

$$P_{\tau\tau} - P_{\chi\chi} - \Omega^2(P_{\chi\chi\tau\tau} - \alpha P_{\tau\tau\tau\tau}) - \epsilon\alpha(P^2)_{\tau\tau} = 0, \quad (21)$$

which is actually a combination of the so-called bad and improved Boussinesq equation (see, e.g., Ref. [29] for the definition and discussion of these models). Travelling wave solutions of the above equation can readily be obtained by introducing the ansatz $P(\chi,\tau) = \Phi(\xi)$, where $\xi = \delta(\tau - \chi/v)$, while v and δ denote the velocity and inverse width of the wave. Then, assuming vanishing boundary conditions for Φ, namely $\Phi \to 0$ as $|\xi| \to \infty$, we derive from Eq. (21) the following ordinary differential equation (ODE) for $\Phi(\xi)$:

$$A\Phi'' + B\Phi - \epsilon\alpha\Phi^2 = 0, \quad (22)$$

where primes denote differentiation with respect to ξ, while $A = \Omega^2(\alpha - 1/v^2)$ and $B = 1 - 1/v^2$. Equation (22) can be seen as an equation of motion of a particle in the presence of the potential $V(\Phi) = (B/2A)\Phi^2 - (\epsilon\alpha/3A)\Phi^3$. A straightforward analysis shows that the only physically relevant solution, with the correct (vanishing) boundary conditions, corresponds to a homoclinic orbit, for $A < 0$, $B > 0$, relevant to the hyperbolic fixed point $\Phi = 3B/2\epsilon\alpha$. This solution reads:

$$P(\chi,\tau) = \left(\frac{\Omega^2}{\epsilon}\right)\left(\frac{6\kappa\delta^2}{1 + 4\delta^2\Omega^2}\right)\text{sech}^2\left[\delta\left(\tau - \frac{\chi}{v}\right)\right], \quad (23)$$

where the velocity is given by $v = [(1 + 4\delta^2\Omega^2)/(1 + 4\alpha\delta^2\Omega^2)]^{1/2}$. Obviously, the above solution is characterized by one free parameter, the inverse width δ. Note that since $\Omega^2/\epsilon \sim 1$ (as per our assumption above), the free parameter δ is also ~ 1. Thus, the normalized pressure P, along with its spectral width, are of the order of unity as well. Using Eq. (23), we can express—for the sake of clarity—the corresponding approximate solution of Eq. (13) in terms of the original space and time coordinates as follows:

$$\frac{p(x,t)}{p_0} \approx \frac{3\kappa\delta^2(\tilde{\omega}_0/\omega_0)^2}{1 + 4\delta^2(\tilde{\omega}_0/\omega_0)^2}\text{sech}^2\left[\delta\tilde{\omega}_0\left(t - \frac{x}{v}\right)\right]. \quad (24)$$

Notice that, in physical units, the velocity of the soliton reads:

$$v = c_0\sqrt{\alpha}\sqrt{\frac{\omega_0^2 + 4\delta^2\tilde{\omega}_0^2}{\omega_0^2 + 4\alpha\delta^2\tilde{\omega}_0^2}}, \quad (25)$$

and is bounded (as follows from the requirements $A < 0$ and $B > 0$ mentioned above) according to:

$$c_0\sqrt{\alpha} < v < c_0. \quad (26)$$

This shows that the velocity of the Boussinesq-type soliton of Eq. (24) is lower than the speed of sound (i.e., the soliton is subsonic), in accordance with the analysis of Ref. [13] for small geometrical factor κ [see Eq. (2.14) of this work].

We have numerically integrated the nonlinear lattice model of Eq. (13), using as an initial condition, p_1 (i.e., the pressure at the first site of the lattice), the functional form of the soliton of Eq. (24) at $x = 0$; we have used the parameter values $\delta\tilde{\omega}_0 = 0.1$ and a cavity length $h = 0.07$ m. The results of our simulations are shown in Fig. 6. The top panel shows a three-dimensional (3D) plot depicting the evolution of the pressure p, while the bottom panel shows the temporal profile of the pressure at the lattice site $n = 60$, corresponding to a physical distance $x = 6$ m. It is observed that the soliton propagates for about 20 m with almost no distortion. In fact, the only noticeable effect is a small amount of radiation emitted by the soliton during its evolution (cf. the structure formed
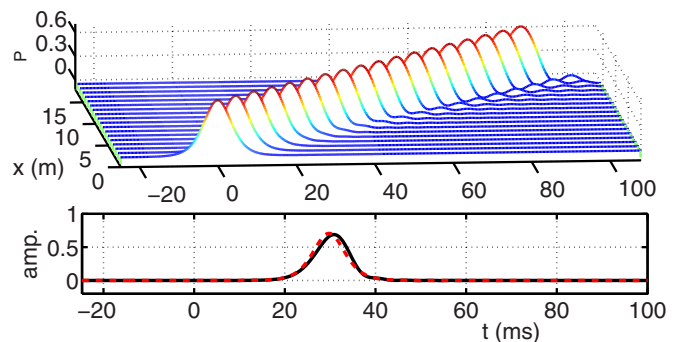

FIG. 6. (Color online) Top panel: Three-dimensional plot depicting the evolution of a soliton of the form of Eq. (23), obtained by numerically integrating Eq. (13) for a distance corresponding to 200 sites (physical distance $x = 20$ m). The bottom panel shows the temporal profile of the normalized pressure, p/p_0, at the site $n = 60$. Parameter values correspond to the experimental ones for a Helmholtz resonator with cavity length $h = 0.07$ m. The dashed (red) line in the bottom panel depicts the analytical result of Eq. (23), while the solid (black) line the result of the simulation.

at the leading edge of the pulse); this effect can naturally be attributed to the fact that Eq. (24) is nothing but an approximate solution—derived in the continuum limit—of the lattice model of Eq. (13). Nevertheless, as is also shown in the bottom panel of Fig. 6, our analytical approximation is very good, at least for propagation distances up to 40 m: Indeed, the analytical result [dashed (red) line] for the soliton profile (at $x = 6$ m) in the bottom panel of the figure almost coincides with the corresponding numerical result [solid (black) line].

For longer propagation distances ($x \gtrsim 40$ m), however, the continuous emission of radiation of the Boussinesq-type solitons eventually lead to their disintegration. More robust soliton solutions—in the same parametric region—can be obtained upon considering the long-wavelength, far-field limit of the Boussinesq-type Eq. (17), which is the KdV equation. Indeed, using a formal multiscale expansion method, we can reduce Eq. (17) to a KdV equation and use the latter to derive approximate solutions of Eq. (13). We thus proceed upon using the slow variables

$$T = \epsilon^{1/2}(\tau - \chi), \qquad X = \epsilon^{3/2}\chi, \tag{27}$$

and express Eq. (17) as follows:

$$2\epsilon^2 P_{XT} - \epsilon^3 P_{XX} - \Omega^2(\epsilon^2 P_{TTTT} - 2\epsilon^3 P_{XX} + \epsilon^4 P_{XX}$$
$$- \alpha\epsilon^2 P_{TTTT}) - \epsilon^2\alpha[(P^2)_{TT} + \epsilon(P^2)_{TTTT}] = 0. \tag{28}$$

Next, introducing the expansion $P = P_1 + \epsilon P_2 + \cdots$, and integrating Eq. (28) once in T, at order $\mathcal{O}(\epsilon^2)$ we obtain the following KdV equation for P_1:

$$P_{1X} - \frac{\Omega^2}{2}(1 - \alpha)P_{1TTT} - \alpha P_1 P_{1T} = 0. \tag{29}$$

To this end, using the soliton solution of Eq. (29) for P_1, namely $P_1 = 6\kappa\Omega^2 \text{sech}^2(T - X/V)$ (where $V^{-1} = 2\Omega^2\kappa\alpha$), we can write the approximate KdV soliton solution for $p(x,t)$ as follows:

$$\frac{p(x,t)}{p_0} \approx 3\epsilon\kappa(\tilde{\omega}_0/\omega_0)^2 \text{sech}^2\left[\sqrt{\epsilon}\tilde{\omega}_0\left(t - \frac{x}{v}\right)\right], \tag{30}$$

where the velocity of the KdV soliton is given by

$$v \approx c_0\sqrt{a}(1 + 2\epsilon\Omega^2\kappa\alpha). \tag{31}$$

It is observed that the amplitude of the normalized pressure p/p_0 is now of order $\epsilon\Omega^2$ and, thus, KdV solitons are of smaller amplitude than the Boussinesq-type solitons [cf. Eq. (23)]. In fact, the KdV soliton (30) can be obtained as the small-amplitude limit of Eq. (23), corresponding to $\delta = \sqrt{\epsilon} \ll 1$ [and, accordingly, the velocity (25) is reduced to (31) in the same limit].

The evolution of the small-amplitude KdV soliton was also studied numerically: In Fig. 7 we show the result of a direct numerical simulation for the same parameters as in Fig. 6, where the initial condition (at the first site as before) for Eq. (13) was the KdV soliton (30) at $x = 0$, with an amplitude $\epsilon\Omega^2 = 0.05$. It is observed that the KdV soliton is much more robust, and no noticeable emission of radiation occurs; this is natural as, in this case, the KdV Eq. (29) is the long-wavelength far-field limit of Eq. (13) as mentioned above. The analytical result for the temporal soliton profile (cf. bottom panel of the figure) is found to be in excellent agreement with the
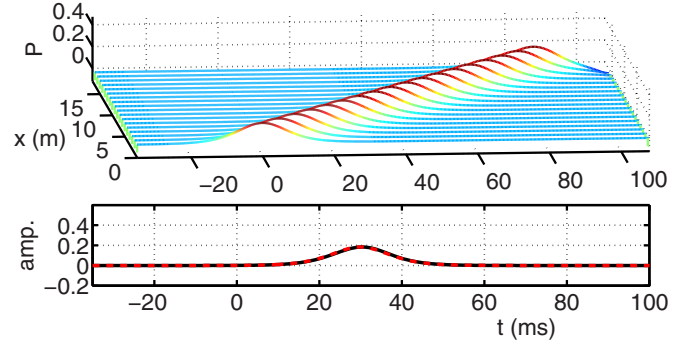

FIG. 7. (Color online) Same as in Fig. 6 but for an initial condition corresponding to a KdV soliton of the form of Eq. (30).

numerically obtained solution. Notice that the KdV solitons were found to be robust for propagation distances of the order of 60 m (which was the distance used in the simulations).

It is interesting to compare the above approximate KdV soliton solution with the corresponding solution discussed in Refs. [11–13]. In both cases, the soliton amplitude is analogous to the square root of the soliton inverse width and analogous to the geometrical factor κ. Additionally, both in our case and in Refs. [11–13], the KdV solitons were obtained in the same asymptotic limit of small amplitude and large width.

We complete this subsection by noting the following: If the initial condition for Eq. (13) is fixed (i.e., the spectral width $\tilde{\omega}_0$ and amplitude are fixed), then the soliton amplitude will also be fixed. Nevertheless, if the cavity length h is increased, then the soliton width $w = (\delta\tilde{\omega}_0)^{-1}$ [cf. Eq. (24)] is also increased (this occurs for both the Boussinesq-like and KdV solitons). This theoretical prediction—which is based on our analytical approximations—is in accordance with the numerical and experimental results shown in Figs. 4 and 2, respectively; for the latter, however, the presence of dissipation results, additionally, in unequal soliton amplitudes.

D. NLS envelope solitons

Our analytical approach allows us to predict still another type of soliton solution, namely *envelope solitons* of the bright and dark type [6], that can be supported in the acoustic waveguide structure under consideration. In particular, in this section we will show that such solitons can be found as approximate solutions of the nonlinear evolution equation (17). Our methodology relies on the use of the multiple scales perturbation method [30], by means of which Eq. (17) is reduced to an effective NLS equation; then, employing the latter, we identify parameter regimes envelope bright or dark acoustic solitons can be formed in our setting.

We start our analysis by introducing the slow variables

$$\chi_n = \epsilon^n\chi, \quad \tau_n = \epsilon^n\tau, \quad n = 0,1,2,\dots, \tag{32}$$

where parameter ϵ is the one appearing in Eq. (17) and will again be treated as a formal small parameter; furthermore, we express P as an asymptotic series in ϵ:

$$P = P_0 + \epsilon P_1 + \epsilon^2 P_2 + \dots, \tag{33}$$

where the unknown real functions P_n ($n = 0,1,2,\dots$) depend on the variables (32). Then, substituting Eq. (33) into Eq. (17),

and using Eq. (32), we obtain a hierarchy of equations at various orders in ϵ (see Appendix).

In particular, at the leading order, i.e., at $\mathcal{O}(1)$, the resulting equation [cf. Eq. (A1) in Appendix] corresponds to the linear limit of Eq. (17); this equation possesses plane-wave solutions of the form:

$$P_0(\tau_0, \chi_0, \tau_1, \chi_1, \ldots) = \Phi(\tau_1, \chi_1, \tau_2, \chi_2, \ldots)$$
$$\times \exp[i\theta(\tau_0, \chi_0)] + \text{c.c.}, \quad (34)$$

where Φ is the unknown envelope function of P_0, the phase $\theta(\tau_0, \chi_0)$ is given by $\theta(\tau_0, \chi_0) = k\chi_0 - \omega\tau_0$, while k and ω satisfy the linear dispersion relation, cf. Eq. (18).

Next, at the order $\mathcal{O}(\epsilon)$, the solvability condition for the corresponding equation [cf. Eq. (A2) in Appendix] is $\tilde{L}_1 P_0 = 0$; this condition is nothing but the requirement that the secular part (which is in resonance with $\tilde{L}_0 P_1$) vanishes. This condition yields the following equation:

$$\left(k' \frac{\partial}{\partial \tau_1} - \frac{\partial}{\partial \chi_1} \right) \Phi(\chi_1, \tau_1, \ldots) = 0, \quad (35)$$

where $k' \equiv \partial k / \partial \omega$ is the inverse group velocity. Equation (35) is satisfied as long as Φ depends on the variables χ_1 and τ_1 through the traveling-wave coordinate $\tilde{\tau}_1 = \tau_1 + k'\chi_1$ (i.e., Φ travels with the group velocity), namely $\Phi(\chi_1, \tau_1, \ldots) = \Phi(\tilde{\tau}_1, \chi_2, \tau_2, \ldots)$. Additionally, at the same order, we obtain the form of the field P_1, namely:

$$P_1 = -\frac{4\alpha\omega^2(1 - 4\Omega^2\omega^2)}{D(2\omega, 2k)} \Phi^2(\tilde{\tau}_1) e^{2i\theta} + Be^{i\theta} + \text{c.c.}, \quad (36)$$

where B is an unknown function that in principle can be found at a higher-order approximation.

Finally, following a similar procedure as above, and using the functional forms of Φ and P_1, the nonsecularity condition of the equation at the order $\mathcal{O}(\epsilon^2)$ [cf. Eq. (A3) in Appendix] yields a NLS equation for the envelope function Φ:

$$i\frac{\partial \Phi}{\partial \chi_2} - \frac{1}{2} k'' \frac{\partial^2 \Phi}{\partial \tilde{\tau}_1^2} + q|\Phi|^2 \Phi = 0, \quad (37)$$

where the dispersion and nonlinearity coefficients are respectively given by:

$$k'' \equiv \frac{\partial^2 k}{\partial \omega^2}$$
$$= \frac{1 - k'^2(1 - \Omega^2\omega^2) + \Omega^2(k^2 - 6\Omega^2\omega^2 - 4\Omega^2\omega kk')}{k(1 - \Omega^2\omega^2)},$$
$$\quad (38)$$

$$q(\omega, k) = \frac{\alpha^2(1 - \Omega^2\omega^2)(1 - 4\Omega^2\omega^2)}{3k\Omega^2(1 - \alpha)}. \quad (39)$$

Importantly, the sign of the product $\sigma \equiv \text{sgn}(qk'')$ determines the nature of the NLS equation, focusing ($\sigma = +1$) or defocusing ($\sigma = -1$), and, hence, the type of the soliton—bright soliton and dark soliton, respectively [6]. In Fig. 8 we show an example of the dependence of the product qk'' with respect to the frequency ω, corresponding to a Helmholtz resonator of a cavity length $h = 0.07$ m. As seen in the figure, there exist two different regimes: the low- (high-) frequency
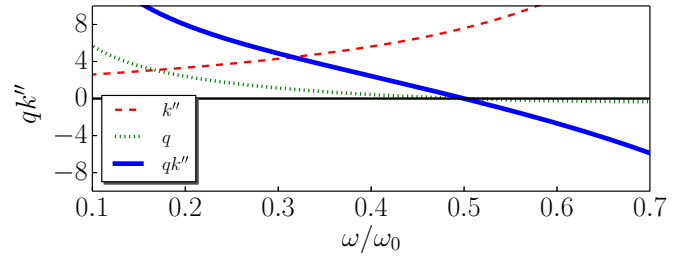

FIG. 8. (Color online) The solid line shows the frequency dependence of the product qk'' of the dispersion and nonlinearity coefficients of the NLS Eq. (37). Dashed and dotted lines shows the frequency dependence of k'' and q, respectively. Parameter values correspond to the experimental ones for a Helmholtz resonator with cavity length $h = 0.07$ m.

regime where $\sigma = +1$ ($\sigma = -1$) and where bright (dark) solitons can be formed.

First, we consider the low-frequency regime of Fig. 8, where the NLS Eq. (37) is focusing and supports an exact analytical bright soliton solution of the form $\Phi = (\eta/\sqrt{q})\text{sech}(\eta/\sqrt{|k''|}\tilde{\tau}_1)\exp[i(\eta^2/2)\chi_2]$. This expression leads to an approximate bright soliton solution of Eq. (17), which is written in terms of coordinates χ and τ as follows:

$$P \approx \frac{2\eta}{\sqrt{q}} \text{sech}\left[\frac{\epsilon\eta}{\sqrt{|k''|}}(\tau + k'\chi) \right]$$
$$\times \cos\left[\omega\tau - \left(k - \frac{\epsilon^2\eta^2}{2} \right)\chi \right]. \quad (40)$$

In terms of the original space and time coordinates, the approximate envelope soliton solution for the pressure p is the following:

$$\frac{p(x, t)}{p_0} \approx \frac{2\epsilon\eta}{\sqrt{q}} \text{sech}\left[\frac{\epsilon\eta}{\sqrt{|k''|}} \left(t + \frac{k'}{c_0\sqrt{\alpha}}\chi \right) \right]$$
$$\times \cos\left[\tilde{\omega}_0 t - \left(\frac{k - (\epsilon^2\eta^2)/2}{c_0\sqrt{\alpha}} \right)x \right], \quad (41)$$

where parameters q, k', and k'', for a given frequency $\tilde{\omega}_0$, are found by using the dispersion relation in the original coordinates.

Next we consider the high-frequency regime of Fig. 8, where the NLS Eq. (37) is defocusing and admits a dark soliton solution of the form $\Phi = \sqrt{\Phi_0}\tanh[\sqrt{\Phi_0/|k''|}\tilde{\tau}_1]\exp(-i\Phi_0\chi_2)$. In this case, the corresponding approximate solution of Eq. (17) reads:

$$P \approx 2\sqrt{\frac{\Phi_0}{q}} \tanh\left[\sqrt{\frac{\Phi_0}{|k''|}}\epsilon(\tau + k'\chi) \right]$$
$$\times \cos[\omega\tau - (k + \epsilon^2\Phi_0)\chi]. \quad (42)$$

Accordingly, the approximate dark envelope soliton solution for the pressure p in the original coordinates is given by:

$$\frac{p(x, t)}{p_0} \approx 2\epsilon\sqrt{\frac{\Phi_0}{q}} \tanh\left[\sqrt{\frac{\Phi_0}{|k''|}}\epsilon\tilde{\omega}_0 \left(t + \frac{k'}{c_0\sqrt{\alpha}}x \right) \right]$$
$$\times \cos\left[\tilde{\omega}_0 t - \left(\frac{k + \epsilon^2\Phi_0}{c_0\sqrt{\alpha}} \right)x \right]. \quad (43)$$
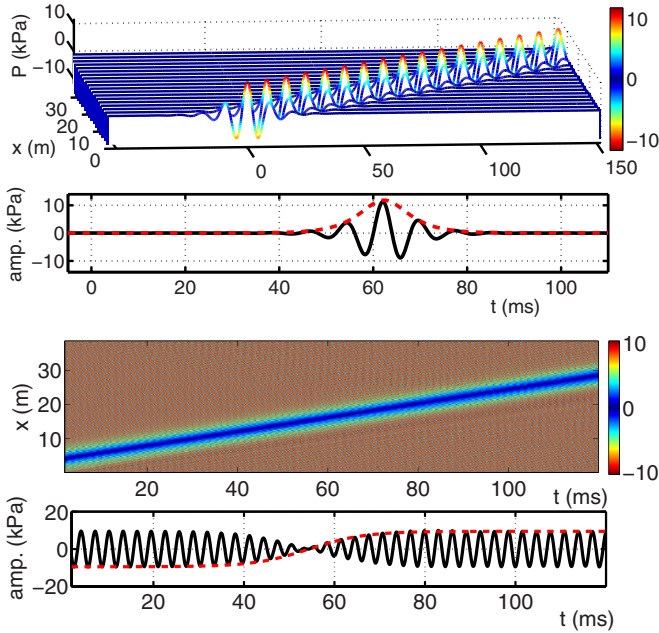
FIG. 9. (Color online) Top panels (bottom panels): Same as in Fig. 6 but for an initial condition corresponding to a bright (dark) NLS soliton of the form of Eq. (41) [Eq. (43)]. In the second (fourth) panel, the dashed (red) line depicts the analytical result for the sech- (tanh-) shaped envelope of Eq. (41) [Eq. (43)]. Parameter values correspond to the experimental ones for a Helmholtz resonator with cavity length $h = 0.07$ m.

Note that both the bright and the dark solitons travel with the group velocity $1/k'$ (evaluated at the frequency $\tilde{\omega}_0$).

Our analytical predictions for the existence of bright and dark solitons in the acoustic waveguide structure at hand were also compared to direct numerical simulations. As in the case of the previous soliton types, we numerically integrated the nonlinear lattice model of Eq. (13) using as initial conditions (at the first lattice site, $n = 0$) the functional forms of the envelope solitons (41) and (43) at $x = 0$. The results are shown in Fig. 9, where the two top (bottom) panels correspond to the bright (dark) soliton, respectively. We have used the following parameter values: $\tilde{\omega}_0 = 0.2\omega_0$ and amplitude $\epsilon\eta = 0.2$ for the bright soliton and $\tilde{\omega}_0 = 0.55\omega_0$ and $\epsilon\sqrt{\Phi_0} = 0.2$ for the dark soliton. In the first and third panels, we show a 3D and a contour plot showing the evolution of these two envelope soliton types, while in the second and fourth panels we show the temporal profiles of the bright and dark solitons at the site $n = 200$ (or $x = 20$ m in physical units). It is observed that the agreement between the numerical results [solid (black) line] obtained in the framework of Eq. (13) and the analytical results [dashed (red) lines depicting the envelopes of the two solitons] is excellent.

IV. CONCLUSIONS AND DISCUSSION

In conclusion, we presented experimental results showing the formation of acoustic pulselike solitons in an air-filled quasi-1D tube with Helmholtz resonators. Additionally, we proposed a transmission line (TL) approach to theoretically study our observations. Our model, which relied on the electroacoustic analogy, was a nonlinear dynamical lattice;

the latter was analyzed by use of both numerical and analytical techniques.

Our numerical simulations produced results that were in qualitative agreement with the experimental findings. On the analytical side, we considered the continuum limit of the lattice model, and showed—by means of dynamical systems and multiscale expansion methods—that it can be reduced to celebrated soliton equations, namely a Boussinesq-type model, a KdV equation, and a NLS equation. Such reductions allowed us to (i) identify parameter regimes and appropriate spatial and temporal scales where different types of solitons can be formed and (ii) derive various soliton solutions in an analytical form. In all cases, the analytical predictions were in excellent agreement with direct simulations and in qualitative agreement with the experimental observations.

In this study, our analytical approximation was simplified, due to the fact that our model did not take into account inherent losses in the system. This simplification, however, allowed us to (a) provide analytical forms of acoustic solitons in the Helmholtz resonator lattice that were not available before (recall that soliton solutions of Refs. [11–13] were presented in an implicit form and in an explicit form only in some asymptotic limits for the lossless case) and (b) predict envelope solitons in the setting under consideration (only dark envelope solitons were previously predicted to occur in cylindrical acoustic waveguide structures [17]). Furthermore, our analytical approximation provides a clear physical picture for the properties of solitons in various parameter regimes and can, in principle, be used for other studies (thanks to the flexibility of our experimental setting)—such as soliton collisions, soliton-defect interactions, soliton propagation in disordered lattices, and so on.

There are many future research directions that may follow this work. The versatility of the experimental setting of the Helmholtz-resonators lattice, followed by the simplicity of the proposed nonlinear TL model, offer an attractive combination for a variety of future research investigations. First, the experimental realization of envelope solitons and a systematic study of their properties is a particularly interesting theme. Also, one could incorporate nonlinear elements in the parallel branch (related to the resonators), as well as losses in the model, and then use asymptotic and perturbative techniques to capture the propagation properties of solitons, also quantitatively. Another interesting direction is the study of soliton formation and propagation in other waveguide structures, proposed or used in the context of acoustic metamaterials, with the use of the nonlinear TL approach. In the same spirit, it would also be particularly challenging to extend our methodology to higher-dimensional settings. Pertinent studies are currently in progress and results will be reported in future publications.

APPENDIX: PERTURBATION EQUATIONS

Here we present the hierarchy of equations in ϵ, resulting from the substitution of Eq. (33) into Eq. (17). More specifically, at the orders $\mathcal{O}(1)$, $\mathcal{O}(\epsilon)$, and $\mathcal{O}(\epsilon^2)$, we respectively obtain the following equations:

$$\tilde{L}_0 P_0 = 0, \tag{A1}$$

$$\tilde{L}_0 P_1 + \tilde{L}_1 P_0 = \tilde{N}_0\big[P_0^2\big], \tag{A2}$$

$$\tilde{L}_0 P_2 + \tilde{L}_1 P_1 + \tilde{L}_2 P_0 = \tilde{N}_0[2P_0 P_1] + \tilde{N}_1\big[P_0^2\big]. \tag{A3}$$

The linear operators $\tilde{L}_0$, $\tilde{L}_1$, and $\tilde{L}_2$, as well as the nonlinear operators $\tilde{N}_0[P]$, $\tilde{N}_1[P]$, are given by:

$$\tilde{L}_0 = \frac{\partial^2}{\partial \tau_0^2} - \frac{\partial^2}{\partial \chi_0^2} - \Omega^2\left(\frac{\partial^4}{\partial \tau_0^2 \partial \chi_0^2} - \alpha \frac{\partial^4}{\partial \tau_0^4}\right), \tag{A4}$$

$$\tilde{L}_1 = 2\frac{\partial^2}{\partial \tau_0 \partial \tau_1} - 2\frac{\partial^2}{\partial \chi_0 \partial \chi_1} - \Omega^2\left(2\frac{\partial^4}{\partial \tau_0^2 \partial \chi_0 \partial \chi_1} + 2\frac{\partial^4}{\partial \chi_0^2 \partial \tau_0 \partial \tau_1} - 4\alpha \frac{\partial^4}{\partial \tau_0^3 \partial \tau_1}\right), \tag{A5}$$

$$\tilde{L}_2 = \frac{\partial^2}{\partial \tau_1^2} - \frac{\partial^2}{\partial \chi_1^2} + 2\frac{\partial^2}{\partial \tau_0 \partial \tau_2} - 2\frac{\partial^2}{\partial \chi_0 \partial \chi_2} - \Omega^2\left[\frac{\partial^4}{\partial \tau_0^2 \partial \chi_1^2} + \frac{\partial^4}{\partial \tau_1^2 \partial \chi_0^2} + 4\frac{\partial^4}{\partial \tau_0 \partial \chi_0 \partial \tau_1 \partial \chi_1} + \frac{2\partial^4}{\partial \tau_0^2 \partial \chi_0 \partial \chi_2}\right.$$
$$\left. + 2\frac{\partial^4}{\partial \chi_0^2 \partial \tau_0 \partial \tau_2} - \alpha\left(6\frac{\partial^4}{\partial \tau_0^2 \partial \tau_1^2} + 4\frac{\partial^4}{\partial \tau_0^3 \partial \tau_2}\right)\right], \tag{A6}$$

$$\tilde{N}_0[P] = \alpha\left[\frac{\partial^2(P)}{\partial \tau_0^2} + \Omega^2 \frac{\partial^4(P)}{\partial \tau_0^4}\right], \tag{A7}$$

$$\tilde{N}_1[P] = \alpha\left[2\frac{\partial^2(P)}{\partial \tau_0 \partial \tau_1} + 4\frac{\partial^4(P)}{\partial \tau_0^3 \partial \tau_1}\right]. \tag{A8}$$

[1] T. Dauxois and M. Peyrard, *Physics of Solitons* (Cambridge University Press, Cambridge, 2006).

[2] M. Remoissenet, *Waves Called Solitons* (Springer, Berlin, 1999).

[3] M. J. Ablowitz, *Nonlinear Dispersive Waves: Asymptotic Analysis and Solitons* (Cambridge University Press, Cambridge, 2011).

[4] R. S. Johnson, *A Modern Introduction to the Mathematical Theory of Water Waves* (Cambridge University Press, Cambridge, 1997).

[5] E. Infeld and G. Rowlands, *Nonlinear Waves, Solitons and Chaos* (Cambridge University Press, Cambridge, 1990).

[6] Yu. S. Kivshar and G. P. Agrawal, *Optical Solitons: From Fibers to Photonic Crystals* (Academic Press, San Diego, 2003).

[7] P. G. Kevrekidis, D. J. Frantzeskakis, and R. Carretero-González, *Emergent Nonlinear Phenomena in Bose-Einstein Condensates: Theory and Experiment* (Springer-Verlag, Heidelberg, 2008); R. Carretero-González, D. J. Frantzeskakis, and P. G. Kevrekidis, Nonlinearity **21**, R139 (2008).

[8] K. Naugolnykh and L. Ostrovsky, *Nonlinear Processes in Acoustics* (Cambridge University Press, Cambridge, 1998).

[9] V. F. Nesterenko, *Dynamics of Heterogeneous Materials* (Springer-Verlag, New York, 2001).

[10] P. Hess and A. M. Lomonosov, Ultasonics **50**, 167 (2010).

[11] N. Sugimoto, J. Fluid Mech. **244**, 55 (1992).

[12] N. Sugimoto, M. Masuda, J. Ohno, and D. Motoi, Phys. Rev. Lett. **83**, 4053 (1999).

[13] N. Sugimoto, M. Masuda, K. Yamashita, and H. Horimoto, J. Fluid Mech. **504**, 271 (2004).

[14] B. Lombard and J. F. Mercier, J. Comput. Phys. **259**, 421 (2014).

[15] P. M. Jordan, Phys. Lett. A **326**, 77 (2004); P. M. Jordan and A. Puri, *ibid.* **335**, 150 (2005); **361**, 529 (2007).

[16] M. Chen, M. Torres, and T. Walsh, Phys. Lett. A **373**, 1037 (2009).

[17] K. Nozaki and T. Taniuti, Physica D **18**, 127 (1986).

[18] O. Richoux, V. Tournat, and T. Le Van Suu, Phys. Rev. E **75**, 026615 (2007).

[19] C. W. Davidson, *Transmission Lines for Communications* (Macmillan, London, 1989).

[20] C. Caloz and T. Itoh, *Electromagnetic Metamaterials: Transmission Line Theory and Microwave Applications* (Wiley, Hoboken, 2006).

[21] F. Bongard, H. Lissek, and J. R. Mosig, Phys. Rev. B **82**, 094306 (2010); Choon Mahn Park, Jong Jin Park, Seung Hwan Lee, Yong Mun Seo, Chul Koo Kim, and Sam H. Lee, Phys. Rev. Lett. **107**, 194301 (2011); Yong Mun Seo, Jong Jin Park, Seung Hwan Lee, Choon Mahn Park, Chul Koo Kim, and Sam Hyeon Lee, J. Appl. Phys. **111**, 023504 (2012); K. J. B. Lee, Myoung Ki Jung, and Sam H. Lee, Phys. Rev. B **86**, 184302 (2012); R. Fleury and A. Alù, Phys. Rev. Lett. **111**, 055501 (2013).

[22] N. Fang, D. Xi, J. Xu, M. Ambati, W. Srituravanich, C. Sun, and X. Zhang, Nat. Mat. **5**, 452 (2006).

[23] Y. Cheng, J. Y. Xu, and X. J. Liu, Phys. Rev. B **77**, 045134 (2008).

[24] A. B. Kozyrev and D. W. van der Weide, J. Phys. D **41**, 173001 (2008); J. Ogasawara and K. Narahara, IEICE Electron. Express **7**, 608 (2010); L. Q. English, S. G. Wheeler, Y. Shen, G. P. Veldes, N. Whitaker, P. G. Kevrekidis, and D. J. Frantzeskakis, Phys. Lett. A **375**, 1242 (2011); Z. Wang, Y. Feng, B. Zhu, J. Zhao, and T. Jiang, J. Appl. Phys. **107**, 094907 (2010); G. P. Veldes, J. Cuevas, P. G. Kevrekidis, and D. J. Frantzeskakis, Phys. Rev. E **83**, 046608 (2011); **88**, 013203 (2013).

[25] L. E. Kinsler, A. U. Frey, A. B. Coppens, and J. V. Sanders, *Fundamentals of Acoustics* (Wiley, New York, 1982); M. Rossi, *Acoustics and Electroacoustics* (Artech House, Norwood, MA, 1988).

[26] O. Richoux, B. Lombard, and J. F. Mercier (unpublished).

[27] M. F. Hamilton and C. L. Morfey, in *Nonlinear Acoustics*, edited by M. F. Hamilton and D. T. Blackstock (Academic Press, San Diego, CA, 1998), Chap. 3.

[28] N. Sugimoto and T. Horioka, J. Acoust. Soc. Am. **97**, 1446 (1995).

[29] P. Rosenau, Phys. Lett. A **118**, 222 (1986).

[30] A. Jeffrey and T. Kawahara, *Asymptotic Methods in Nonlinear Wave Theory* (Pitman, Boston, 1982).